



Large-eddy simulations of contrails in a turbulent atmosphere

J. Picot¹, R. Paoli¹, O. Thouron¹, and D. Cariolle^{1,2}

¹CNRS/CERFACS, URA 1875, Sciences de l'Univers au CERFACS, Toulouse, France

²Météo France, Toulouse, France

Received: 7 October 2014 – Accepted: 27 October 2014 – Published: 27 November 2014

Correspondence to: R. Paoli (paoli@cerfacs.fr)

Published by Copernicus Publications on behalf of the European Geosciences Union.

Title Page

Abstract

Introduction

Conclusions

References

Tables

Figures



Back

Close

Full Screen / Esc

Printer-friendly Version

Interactive Discussion



Abstract

In this work, the evolution of contrails in the vortex and dissipation regimes is studied by means of fully three-dimensional large-eddy simulation (LES) coupled to a Lagrangian particle tracking method to treat the ice phase. This is the first paper where fine-scale atmospheric turbulence is generated and sustained by means of a stochastic forcing that mimics the properties of stably stratified turbulent flows as those occurring in the upper troposphere lower stratosphere. The initial flow-field is composed by the turbulent background flow and a wake flow obtained from separate LES of the jet regime. Atmospheric turbulence is the main driver of the wake instability and the structure of the resulting wake is sensitive to the intensity of the perturbations, primarily in the vertical direction. A stronger turbulence accelerates the onset of the instability, which results in shorter contrail decent and more effective mixing in the interior of the plume. However, the self-induced turbulence that is produced in the wake after the vortex break-up dominates over background turbulence at the end of the vortex regime and dominates the mixing with ambient air. This results in global microphysical characteristics such as ice mass and optical depth that are be slightly affected by the intensity of atmospheric turbulence. On the other hand, the background humidity and temperature have a first order effect on the survival of ice crystals and particle size distribution, which is in line with recent and ongoing studies in the literature.

1 Introduction

Aircraft-induced cloudiness in the form of condensation trails (contrails) and contrail cirrus is among the most uncertain contributors of aviation to the Earth radiative forcing (Lee et al., 2009). One of the main reasons of this uncertainty is the large disparity of scales that exists between the near-field of aircraft engines where emissions are produced, and the grid-boxes of global models that are used to evaluate their global atmospheric impact (Burkhardt et al., 2010). In order to bridge this gap and develop more

ACPD

14, 29499–29546, 2014

LES of contrails in turbulent atmosphere

J. Picot et al.

Title Page

Abstract

Introduction

Conclusions

References

Tables

Figures

◀

▶

◀

▶

Back

Close

Full Screen / Esc

Printer-friendly Version

Interactive Discussion



LES of contrails in
turbulent atmosphere

J. Picot et al.

Title Page

Abstract

Introduction

Conclusions

References

Tables

Figures

I◀

▶I

◀

▶

Back

Close

Full Screen / Esc

Printer-friendly Version

Interactive Discussion



refined parameterizations of unresolved plume processes into global models, one has to gain better knowledge of the dynamical and the microphysical properties of contrails and their precursors. For that purpose, high-fidelity numerical simulations such as large-eddy simulations (LES) are now becoming a reliable instrument of research in the atmospheric science community as they allow for an accurate description of the physicochemical processes that occur in aircraft wakes (Unterstrasser and Gierens, 2010a; Paugam et al., 2010; Naiman et al., 2011).

According to the classification made by Gerz et al. (1998), the wake of an aircraft can be split into four successive regimes: during the first few seconds after emission (jet regime), ice forms by condensation of water vapor onto particle nucleation sites like soot emitted by the engines (Schumann, 1996; Kärcher et al., 1996), while the vorticity shed by the aircraft wings rolls up into a pair of counter-rotating vortices where the ice and vapor exhausts are trapped (primary wake). In the following minutes (vortex regime), the primary wake descends because of the downward motion induced by the vortices on each other; then it interacts with the surrounding atmosphere via a baroclinic instability, which eventually leads to the formation of an upward-moving secondary wake (Spalart, 1996) where part of the exhausts and ice particles are detrained (Gerz and Ehret, 1997). The vortices also interact with each other via mutual instability (Crow, 1970; Widnall et al., 1974) until they break up and release the exhaust in the atmosphere (dissipation regime). For high ambient humidity ice particles size can increase dramatically by condensation of ambient water vapor (Lewellen and Lewellen, 2001; Paugam et al., 2010; Naiman et al., 2011). During the final diffusion regime, the contrail evolution is controlled by atmospheric motion via shear and turbulence (Gerz et al., 1998), and by radiative transfer processes and sedimentation (Unterstrasser and Gierens, 2010a, b) until complete mixing usually within a few hours.

From a computational perspective, the vortex regime is particularly challenging because of the intricate transformations that occur in the wake and changes in the flow topology, which manifest as abrupt expansions of the contrail in both horizontal and vertical directions (Sussmann, 1999). These transformations necessarily affect the ice

LES of contrails in
turbulent atmosphere

J. Picot et al.

Title Page

Abstract

Introduction

Conclusions

References

Tables

Figures

◀

▶

◀

▶

Back

Close

Full Screen / Esc

Printer-friendly Version

Interactive Discussion



microphysical properties. Most of numerical simulations of contrails in the vortex regime in the literature rely on Eulerian formulations for the treatment of ice particles. For example Lewellen and Lewellen (2001), Huebsch and Lewellen (2006) and Paugam et al. (2010) used three-dimensional LES with different levels of sophistication of ice microphysics, different set-ups of the dynamics and different resolution to cover timescales beyond the end of the vortex regime. The results of these studies showed that ambient humidity, stratification and turbulence are among the factors controlling the survival of ice crystals and their spatial distribution at the end of the vortex regime. These findings have been confirmed by LES coupled to a Lagrangian Particle Tracking (LPT) method in three-dimensional (Naiman et al., 2011) and two-dimensional frameworks (Unterstrasser and Sölch, 2010), respectively. The latter authors also compared the results obtained with Eulerian and Lagrangian based methods on the same computational grid and observed that the LPT allow for a more accurate representation of ice microphysics. This aspect was recently investigated by Unterstrasser et al. (2014) in the context of tracer dispersion in aircraft wake vortices. They observed that LPT appears to be less dissipative than Eulerian formulations in reproducing particle dispersion in aircraft wake vortices although this conclusion has to be taken with caution because it is quite sensitive to the accuracy of the numerical scheme and the computational grid.

An aspect that has not been fully investigated so far is the role of atmospheric turbulence in determining the three-dimensional structure of contrails and the ice microphysical properties. For example, it is likely that turbulence enhances the mixing of ice crystals with atmospheric water vapor, especially in the secondary wake, and it influences the detrainment of exhausts at the vortex boundaries. In addition, vortex instabilities such as Crow instability (Crow, 1970) or elliptical instability (Widnall et al., 1974) can be triggered by atmospheric turbulence, which ultimately lead to their break-up and decay. Unterstrasser et al. (2008) used 2-D LES with modified diffusion of the vortex core to mimic the effects of three-dimensional vortex decay in a turbulent environment, a procedure that was also used by Unterstrasser and Gierens (2010a) and Unterstrasser and Sölch (2010). Lewellen et al. (2014) recently proposed a “quasi-3-D”

LES of contrails in
turbulent atmosphere

J. Picot et al.

Title Page

Abstract

Introduction

Conclusions

References

Tables

Figures

I◀

▶I

◀

▶

Back

Close

Full Screen / Esc

Printer-friendly Version

Interactive Discussion



approach which consists in resolving a certain narrow range of 3-D eddies that are imposed a priori rather than emerging naturally from the turbulent cascade. Comparisons of global contrail parameters with those obtained using full 3-D LES were reported to be satisfactory for selected case studies. While the procedures described above are fast and suitable for sensitivity analysis of global contrail properties to background turbulence, the treatment of vortex dynamics and the representation of atmospheric turbulence remain strongly parametrized. In fully 3-D LES of contrail realized to date, turbulence models have been mainly used to trigger vortex instabilities rather than investigate the effects of background turbulence on the wake structure and the contrail properties. Paugam et al. (2010) introduced rather idealized perturbations in the form of sine waves, while Naiman et al. (2011), Lewellen et al. (2014), and Unterstrasser (2014) used divergence-free random fields with imposed spectrum which are evolved in order to develop coherent turbulent eddies that constitute the initial condition for the contrail simulations. However, during this transient time turbulence decays, which makes difficult to control the level of the atmospheric turbulence that effectively interacts with the wake vortices.

This work is part of a larger project that aims at evaluating the atmospheric impact of contrail cirrus using a systematic chain of models and LES computations that cover the contrail lifetime from the formation to its demise in the atmosphere. While this strategy is similar to that employed recently by other authors who explored a large set of parameter space (Lewellen et al., 2014; Unterstrasser, 2014), the present paper focuses on a specific point that is the fine-scale description of atmospheric turbulence and its effects on the mechanics of the wake and the contrail physics during the vortex phase – preliminary results of this work were presented by Picot et al. (2012). To that end, turbulence is generated by means of a spectral stochastic forcing technique that allows the nonlinear turbulent cascade to develop at smaller scales and was specially devised for strongly stratified turbulent flows as those occurring in the upper troposphere lower stratosphere (UTLS) (Paoli and Shariff, 2009; Paoli et al., 2014). To the authors knowledge, this is the first time such sophisticated treatment of atmospheric

LES of contrails in
turbulent atmosphere

J. Picot et al.

Title Page

Abstract

Introduction

Conclusions

References

Tables

Figures

◀

▶

◀

▶

Back

Close

Full Screen / Esc

Printer-friendly Version

Interactive Discussion



turbulence is employed for contrail simulations. This point is crucial to have a correct representation of turbulence that is strongly anisotropic and hence substantially different and more complex than classical Kolmogorov turbulence. The application of the forcing technique to the UTLS turbulence is described in the LES by Paoli et al. (2014) where the statistical proprieties were analyzed and compared with theoretical analysis of strongly stratified flows (Brethouwer et al., 2007). The study showed that a substantial amount of turbulent kinetic energy is present at sub-kilometer scales relevant to the wake flow dynamics, which have then to be properly resolved. In particular, the LES data revealed the typical flow structures characterized by horizontally layered eddies or “pancakes” (Riley and Lelong, 2000) that are a signature of the background field used for the present contrail simulations. The initial wake-flow field is also based on data from LES of the jet regime at a wake age of 10 s that takes into account the jet/vortex interaction process (Paoli et al., 2013). In addition, the numerical model uses a fully 3-D Lagrangian approach to track the crystals. Since turbulence can be fully controlled, this methodology allows for a sensitivity analysis of the wake and contrail properties in the vortex regime as a function of turbulence intensity. The sensitivity to background humidity and temperature is also discussed and compared to the sensitivity to turbulence. The paper is organized as follows: Sect. 2 summarizes the model equations, Sect. 3 describes computational setup of the simulations, and Sect. 4 presents the results of the simulations. Conclusions are drawn in Sect. 5.

2 Model equations

The computational model used in this work is based on an Eulerian–Lagrangian approach: the large-scale eddies of the gaseous atmosphere are solved with compressible Navier–Stokes equations, while ice crystals are treated by a Lagrangian tracking method and mass transfer between the two phases. As this model has already been presented elsewhere (Paoli et al., 2008, 2013), only a summary is presented here. The density ρ , velocity \mathbf{u} , total energy $E = C_v T + \frac{1}{2} \mathbf{u}^2$ (where T is the temperature) and water

vapor mass fraction Y_v are solution of the Favre-filtered Navier–Stokes equations:

$$\frac{\partial \rho}{\partial t} + \nabla \cdot (\rho \mathbf{u}) = \omega_v, \quad (1a)$$

$$\frac{\partial \rho \mathbf{u}}{\partial t} + \nabla \cdot (\rho \mathbf{u} \otimes \mathbf{u}) + \nabla p = \nabla \cdot \mathbf{T} + \rho \mathbf{g}, \quad (1b)$$

$$\frac{\partial \rho E}{\partial t} + \nabla \cdot ((\rho E + p) \mathbf{u}) = \nabla \cdot (\mathbf{T} \mathbf{u}) + \rho \mathbf{g} \cdot \mathbf{u} - \nabla \cdot \mathbf{q}, \quad (1c)$$

$$\frac{\partial \rho Y_v}{\partial t} + \nabla \cdot (\rho Y_v \mathbf{u}) = -\nabla \cdot \xi + \omega_v, \quad (1d)$$

where the source term ω_v in Eqs. (1a) and (1d) represents the mass transfer between vapor and ice phases detailed in Sect. 2.1; the tensor $\mathbf{T} = 2\mu (\mathbf{S} - \frac{1}{3} S_{kk} \mathbf{1})$ is the shear stress with $\mathbf{S} = \frac{1}{2} (\nabla \mathbf{u} + \nabla \mathbf{u}^T)$, $\mu = \mu_{\text{mol}} + \mu_{\text{sgs}}$ where μ_{mol} and μ_{sgs} are, respectively, the molecular viscosity of air (mol) and the sub-grid scale (sgs) viscosity, the latter obtained from the filtered structure function model by (Ducros et al., 1996); the vector \mathbf{g} is the gravitational acceleration; the pressure p is obtained from the perfect gas law $p = \rho R T$ with R the gas constant for air; the vectors $\mathbf{q} = \mathbf{q}_{\text{mol}} + \mathbf{q}_{\text{sgs}}$ and $\xi = \xi_{\text{mol}} + \xi_{\text{sgs}}$ are the heat and vapor diffusion fluxes, respectively, each one composed of the molecular and sgs fluxes. Given the high Reynolds number flows considered in this study, the molecular transport are small compared to the turbulent transport so that in practice $\mu \simeq \mu_{\text{sgs}}$, $\mathbf{q} \simeq \mathbf{q}_{\text{sgs}}$ and $\xi \simeq \xi_{\text{sgs}}$. These are related to the gradient of temperature and vapor mass fraction by means of turbulent Prandtl and Schmidt numbers: $\mathbf{q}_{\text{sgs}} = -C_p \frac{\mu_{\text{sgs}}}{Pr_t} \nabla T$ and $\xi_{\text{sgs}} = -\frac{\mu_{\text{sgs}}}{Sc_t} \nabla Y_v$. For typical atmospheric flows Pr and Sc depends on Richardson number and other atmospheric parameters (see e.g. Schumann and Gerz, 1995), however at the resolution of $\mathcal{O}(1\text{m})$ considered of here (see Table 1) the subgrid-scale turbulence can be considered isotropic (the Ozmidov scale in the UTLS is one order of magnitude larger, see e.g. Brethouwer et al., 2007) and they are taken constant with values $Pr_t = Sc_t = 0.419$ as in Gerz and Holzäpfel (1999).



Equations (1) are discretized on collocated, Cartesian meshes with non-uniform grid spacing. The spatial derivatives are computed with a sixth-order compact scheme (Lele, 1992) while selective dissipation (Tam and Webb, 1993) enforces numerical stability. Finally, time integration is performed by a third-order Runge–Kutta method with a Courant–Friedrichs–Lewy number fixed to $CFL = 0.5$.

2.1 Ice model

The model uses a Lagrangian approach to track the trajectories of particles: ice crystals and nucleation sites (soot particles emitted by engines in the present study) onto which ice forms by deposition of water vapor. Given the large soot emission index $El_s = \mathcal{O}(10^5) \text{ kg-fuel}^{-1}$ (Kärcher and Yu, 2009), it would be prohibitive to track all soot particles in the wake, so only a reduced number of numerical particles are tracked by the model. A numerical particle represents a cluster of $n_c = n/n_p$ (identical) physical particles that have mass m_p , center of mass \mathbf{x}_p and velocity \mathbf{u}_p . As particles remain small compared to flows structures, the point-force approximation (Boivin et al., 1998) can be used for particle-flow interactions, which means that all fluid properties at particle position are obtained through an interpolation of the values at neighborhood grid points:

$$\frac{d\mathbf{x}_p}{dt} = \mathbf{u}_p, \quad p = 1, \dots, n_p, \quad (2a)$$

$$\frac{d\mathbf{u}_p}{dt} = -\frac{\mathbf{u}_p - \mathbf{u}(\mathbf{x}_p)}{\tau_p} + \mathbf{g}, \quad p = 1, \dots, n_p \quad (2b)$$

where the relaxation time τ_p takes into account the aerodynamic drag of the numerical particle

$$\tau_p = \frac{\rho_{ice} d_p^2}{18\mu_{mol}} \frac{1}{1 + 0.15 Re_p^{0.687}}, \quad Re_p = \frac{\rho d_p}{\mu_{mol}} \|\mathbf{u}_p - \mathbf{u}(\mathbf{x}_p)\| \quad (3)$$

29506



where $\rho_{\text{ice}} = 917 \text{ kg m}^{-3}$ is the density of ice and Re_p is the Reynolds number of the particle. The mass of vapor removed through deposition is

$$-\omega_v(\mathbf{x}) = \sum_p n_c \frac{dm_p}{dt} \delta(\mathbf{x} - \mathbf{x}_p) \quad (4)$$

where δ is the Dirac delta function. In numerical applications, the vapor mass must be removed from the nodes surrounding a numerical particles in order to conserve the total mass, which is done by replacing δ in Eq. (4) by a weighting function that depends on the inverse distance between the node and the particle (Boivin et al., 1998). Similar budgets can be established with drag momentum and thermal exchanges, but they are neglected in Eq. (1) because the mass ratio between ice and gaseous phases remain small.

To close the problem a model for the deposition rate dm_p/dt is needed in Eq. (4). The formation of nucleation sites is the result of complex microphysical processes that are beyond the scope of the present study (Kärcher et al., 1998). In a simplified picture, for a nucleation site to be activated, the air surrounding the particle needs to be saturated with respect to water to form a supercooled droplet that freeze afterwards. The time needed for this freezing depends on the particle size among other parameters but this is in general much smaller than the time step used for fluid dynamics simulations. Hence, as done in previous LES we assume instantaneous freezing (Unterstrasser and Sölch, 2010; Naiman et al., 2011; Paoli et al., 2013). This newly formed crystal subsequently grows by deposition of water vapor. Hence, in the present model, activation is represented by the flag

$$H_p^{\text{act}} = \begin{cases} 1 & \text{if } m_p > 0 \text{ or } Y_v(\mathbf{x}_p) \geq Y_{v,p}^{\text{s,w}} \\ 0 & \text{else} \end{cases} \quad (5)$$

where $Y_{v,p}^{\text{s,w}} = Y_v^{\text{s,w}}(T(\mathbf{x}_p))$ and $Y_v^{\text{s,w}}$ is the equilibrium specific humidity with respect to water. This picture is consistent with recent studies (Kärcher and Yu, 2009) showing

that in the soot-rich regimes as those characterizing modern turbofans, the activation is a thermodynamically-controlled process. The deposition process is obtained by assuming spherical crystals of diameter d_p , i. e.

$$m_p = \frac{\pi}{6} \rho_{ice} d_p^3 \quad (6)$$

- 5 where the soot core size (of the order of nanometers) can be neglected compared to the mass of deposited ice. The deposition rate is (Kärcher et al., 1996)

$$\frac{dm_p}{dt} = H_p^{act} \frac{\pi}{2} d_p G(Kn_p) D_{v,p} \rho(\mathbf{x}_p) (Y_v(\mathbf{x}_p) - Y_{v,p}^{s,i}) \quad (7)$$

- 10 where $Kn_p = 2\lambda_{v,p}/d_p$ is the Knudsen number of the particle; $Y_{v,p}^{s,i} = Y_v^{s,i}(T(\mathbf{x}_p))$ and $Y_v^{s,i}$ is the equilibrium specific humidity with respect to ice; the collisional factor G accounts for the transition from gas kinetic to continuum regime (Kärcher et al., 1996)

$$G(Kn_p) = \left(\frac{1}{1 + Kn_p} + \frac{4}{3} \frac{Kn_p}{\alpha} \right)^{-1} \quad (8)$$

- 15 where the accommodation factor is taken $\alpha = 0.5$, the upper limit of the analysis by Kärcher et al. (1996) (we did not explore the sensitivity to this parameter in this study); the mean free path of vapor molecules in air $\lambda_{v,p} = \lambda_v(p(\mathbf{x}_p), T(\mathbf{x}_p))$ and the diffusion coefficient of vapor in air $D_{v,p} = D_v(p(\mathbf{x}_p), T(\mathbf{x}_p))$ are computed with relations that explicitly account for the dependence on pressure and temperature (Pruppacher and Klett, 1997)

$$\lambda_v(p, T) = \lambda_v^o \left(\frac{p^o}{p} \right) \left(\frac{T}{T^o} \right), \quad (9)$$

$$D_v(p, T) = D_v^o \left(\frac{p^o}{p} \right) \left(\frac{T}{T^o} \right)^{1.94} \quad (10)$$

and transverse direction respectively. In the vertical direction, all flow variables are relaxed toward a thermodynamic state representative of a stratified atmosphere with a uniform Brunt–Väisälä frequency (Paoli et al., 2013). The initial condition consists of an atmospheric flow-field onto which the wake of the aircraft is inserted.

- 5 The background atmosphere is representative of an upper troposphere lower stratosphere region, i. e. stably stratified. The background thermodynamic variables T_b , ρ_b and $\rho_b = \rho_b/(RT_b)$ depend on z and satisfy the relations

$$\frac{N^2}{g} = \frac{1}{\theta_b} \frac{d\theta_b}{dz}, \quad (12a)$$

$$\frac{d\rho_b}{dz} = -\rho_b g \quad (12b)$$

- 10 where $N = 0.012 \text{ s}^{-1}$ is the Brunt–Väisälä frequency while θ_b is the background potential temperature defined by

$$\frac{\theta_b}{\rho_\theta^{(\gamma-1)/\gamma}} = \frac{T_b}{\rho_b^{(\gamma-1)/\gamma}}, \quad (13)$$

- 15 where $\rho_\theta = 10^5 \text{ Pa}$ and $\gamma = 1.4$ is the ratio of specific heats for air. Pressure and density at flight level are kept fixed at $\rho_b(z_0) = \rho_0 = 242.86 \text{ hPa}$ and $\rho_b(z_0) = \rho_0 = 0.3881 \text{ m}^3 \text{ s}^{-1}$ while temperature at flight level $T_b(z_0) = T_0$ is varied to analyze the effects of temperature on contrail properties (see Table 2). The background specific humidity $Y_{v,b}$ is chosen to keep vapor saturation with respect to ice s_0 constant in the computational domain: $Y_{v,b}(z) = s_0 Y_v^{s,i}(T_b(z))$. Vapor saturation s_0 is also varied to analyze the effects of humidity on contrail properties. Atmospheric (or background) turbulence flow-fields were provided by separate LES of such stratified flows with specific eddy dissipation rate ϵ . Because of atmospheric stratification, turbulence is organized in horizontally layered structures, reflecting the strong anisotropy of turbulent fluctuations between
- 20

horizontal and vertical directions as shown in Fig. 2. The initial turbulent fields for the present simulations were extracted from the larger computational domain as shown by the black box in Fig. 2.

The initial wake of the aircraft is reconstructed using data from simulations of the jet regime at a wake age of $t = 10$ s (Paoli et al., 2013). These simulations are representative of a B747 aircraft in cruise conditions, i. e. composed of a pair of counter-rotating vortices and engine emissions including vapor and nucleation sites. Each vortex has a circulation of $\Gamma = 565 \text{ m}^2 \text{ s}^{-1}$, a core radius $r_c = 4$ m, and the vortices are spaced by $b = 47$ m. The mass of vapor emitted per meter of flight is $m_{v,e} = 3.75 \text{ g m}^{-1}$ per engine and the number of nucleation sites emitted per meter of flight is $n_e = 10^{12} \text{ m}^{-1}$. Thus, the number of nucleation sites in the computational domain is $n = n_e L_z$, although the number of numerical particles is $n_p = 2 \times 10^6$. At this wake age all particles are already activated. In order to characterize the interaction between background turbulence and vortex dynamics, it is useful to introduce the relative turbulence intensity η_0 that represents the velocity ratio between turbulent fluctuations and vortex descent velocity (Crow and Bate, 1976):

$$\eta_0 = \frac{v_b}{w_0} = \frac{2\pi}{\Gamma} \sqrt[3]{\epsilon b^4}. \quad (14)$$

The simulations have been organized as follows: the reference simulation, labeled case 2, is based on a supersaturated atmosphere at $s_0 = 130\%$, $T_0 = 218 \text{ K}$, and “mild” turbulence intensity. The background turbulence field has been changed in cases 1 and 3 with “strong” and “weak” turbulence intensity, respectively (this nomenclature is the same used by Paoli et al., 2014). Saturation has been reduced in case 4 and 5 to $s_0 = 110\%$ and $s_0 = 95\%$, respectively. Finally, temperature has been reduced in case 6 to $T_0 = 215 \text{ K}$. All simulations parameters are summarized in Tables 1 and 2.



4 Results

4.1 Dynamics of wake vortices

Wake vortices are detected using the λ_2 field, which is defined as the second eigenvalue of the symmetric tensor $\mathbf{S}^2 + \mathbf{\Omega}^2$ with \mathbf{S} and $\mathbf{\Omega}$ being the symmetric and the antisymmetric parts of the velocity gradient tensor, respectively (Jeong and Hussain, 1995). The vortex cores are characterized by negative values of λ_2 with lower values corresponding to stronger vortices. The initial minimum value of λ_2 is found in the flow region inside the wake vortices, $\lambda_{2,0} = \min_{x,y,z} \{\lambda_2(x,y,z;0)\} = -49.67 \text{ s}^{-2}$, which is much smaller than the value corresponding to the vortex tubes of atmospheric turbulence, $\lambda_2^{\text{atm}} = -0.001 \text{ s}^{-2}$. The evolution of λ_2 iso-surfaces reported in Fig. 3 illustrates the mechanism of vortex instability for the reference case. It is known from stability analysis that counter-rotating vortices are prone to both long-wave (Crow) instability with wavelength $\lambda_{\text{lw}} = 8.6b$, and short-wave (elliptical) instability with wavelength $\lambda_{\text{sw}} = 0.37b$ (Crow, 1970; Widnall et al., 1970). For the present study, these values are $\lambda_{\text{lw}} = 405 \text{ m}$ and $\lambda_{\text{sw}} = 17.4 \text{ m}$, respectively. The vortical structures identifying the wake vortices and the background turbulence are characterized by the values $\lambda_2 = \lambda_{2,0}/10$ and $\lambda_2 = \lambda_{2,0}/400\,000 \approx \lambda_2^{\text{atm}}/10$, respectively. The figure shows that turbulence triggers perturbations of the wake vortex system that develop until the two vortex tubes collide and break up. The largest flow structure corresponds to the size of the axial domain, and can then be identified with λ_{lw} . Starting at $t = 2.0 \text{ min}$, the vortex tubes start to get closer and eventually collide at $t = 2.2 \text{ min}$ at two axial locations, $x = 250 \text{ m}$ and $x = 350 \text{ m}$. In the other simulations, a single collision between the vortex tubes is observed, see Fig. 4. It is also interesting to observe the emergence of another flow structure with wavelength of about 25 m starting at $t = 1 \text{ min}$, which can be identified with a short-wave instability. Although this has a higher growth rate (Widnall et al., 1970) than the long-wave instability, in the present case it is not sufficiently strong to overwhelm it and break the vortices before the latter develops.



LES of contrails in
turbulent atmosphere

J. Picot et al.

Title Page

Abstract

Introduction

Conclusions

References

Tables

Figures

I◀

▶I

◀

▶

Back

Close

Full Screen / Esc

Printer-friendly Version

Interactive Discussion



Various numerical simulations in the past showed similar results, eventually highlighting larger or stronger structures of elliptical instability that compete with Crow instability to break up the vortices. Indeed, the ratio between the amplitude of the two types of instability also depends on the topology of the initial perturbation. The simulations mentioned above used distinct perturbation techniques for each type of instability: white noise or homogeneous isotropic turbulence for the short-wave instability, and sinusoidal waves or anisotropic turbulence for the long-wave instability. In the present work the instability is triggered solely by atmospheric turbulence, so that most of the kinetic energy of the initial perturbation is contained in the largest eddies that are commensurate with long-wave rather than short-wave instability. This approach has been used in the vast wake vortex literature and particularly in the studies that attempted to analyze the interaction of the wake with the background turbulence (Lewellen and Lewellen, 1996; Han et al., 2000; Holzäpfel et al., 2001) and more recently by Hennemann and Holzäpfel (2011) and Misaka et al. (2012) who focused on the passive scalar transport in the wake. The main difference with the present study is that here the background turbulence is sustained, yet the 3-D snapshots shown in these studies as well as the various pictures of wake instabilities reported in the literature Crow (1970); Chevalier (1973); Sussmann and Gierens (1999) corroborate the structures visualized in Fig. 3. Isometric views of iso-surfaces $\lambda_2 = \lambda_{2,0}/10$ and $\lambda_2 = \lambda_{2,0}/1\,000$ are drawn in Fig. 4 for cases 1, 2, 3, and 6 taken immediately before and after the vortex tubes collide. The snapshots are similar for the three cases, except for the double collision appearing in case 2, which insures the reproducibility of these flow structures by the present LES. In general, the vortex break-up always starts in the lowermost part of the wake because the wake descent is inversely proportional to the vortex separation (which goes to zero at the collision point).

In order to measure the lifespan of wake vortices, their intensities are evaluated as a function of time: the minimum value of λ_2 of each vortex is measured along the longitudinal axis. The condition $\lambda_2 < \lambda_{2,0}/10$ is used to discriminate wake vortices from secondary vortices. Noticing on Fig. 4 that this condition may not be reached in some

LES of contrails in
turbulent atmosphere

J. Picot et al.

Title Page

Abstract

Introduction

Conclusions

References

Tables

Figures

◀

▶

◀

▶

Back

Close

Full Screen / Esc

Printer-friendly Version

Interactive Discussion



parts of the longitudinal axis, we define the vortex length x_v as the length of the longitudinal axis covering all axial sections where this condition is verified. The length ratio x_v/L_x and the average vortex intensity $\bar{\lambda}_2$ are plotted in Fig. 5 for each vortex and for cases 1, 2, 3, and 6. The magnitude of $\bar{\lambda}_2$ quickly decreases at the beginning, then its rate of variation stabilizes at a constant value of $-0.1|\lambda_{2,0}|$ per minute. The ratio x_v/L_x is initially equal to 1, meaning that coherent vortices can be detectable over all the axial domain. After a couple of minutes, the magnitude of $\bar{\lambda}_2$ decreases abruptly and falls below $-|\lambda_{2,0}|/10$ within a few seconds. In the meantime, x_v decreases and reaches zero within the same time span. The abrupt slope change is the mark of the vortex break-up as shown by snapshots of Fig. 4, which are taken at the times indicated by the vertical dashed lines in Fig. 5. The wake lifespan t_b is defined by the abrupt slope change and values are given in Table 3. The results obtained for all cases studied are compared in Fig. 6 to the analytical estimation of Crow and Bate (1976) and contrasted with a limited set of measurements and numerical data found in the literature (Crow and Bate, 1976; Spalart and Wray, 1996). In spite of the large scatter of data (even with similar turbulence level), the numerical values of t_b are in the range of experimental values. All collected data show a similar trend: weaker relative turbulence leads to longer lifespan (as observed for example by Holzäpfel, 2003). Similar trends were recently reported using the normalized Brunt–Väisälä frequency $N^* = N t_0$ and the vortex sinking distance $z_b = w_0 \times t_b$ instead of the vortex lifespan t_b (Schumann, 2012; Jeßberger et al., 2013; Schumann et al., 2013) and Fig. 7 shows a general good agreement with those data.

In order to evaluate the vertical displacement of the wake vortices, vertical profiles $\tilde{\lambda}_2(z, t) = \min_{x,y} \{\lambda_2(x, y, z; t)\}$ are taken at different times and shown in Fig. 8. They descend roughly 100 m after $t = 1$ min, in agreement with previous observational studies (Sussmann and Gierens, 1999). The minimum values of λ_2 are coherent with values found in Fig. 5 and indicate the region containing the vortices. The vertical spread of this region increases at a rate of 20 m min^{-1} , which is due to the development of instabilities discussed in Fig. 3. We observed in Fig. 4 that the vertical displacement increases

in the regions where the vortex separation goes to zero, this phenomenon is observed again in Fig. 8 as the vertical spreading has accelerated at $t = 2$ min in cases 1, 3, 6. Besides, the minimum value of $\tilde{\lambda}_2$ has increased towards zero in cases 1, 3 in accordance with Fig. 5. At the end of the vortex regime, the primary wake is found between 200 m and 300 m below flight level.

4.2 Contrail microphysics

As explained in Sect. 2.1, vapor deposits on ice crystals at a rate that depends on the local ice supersaturation. This process is represented in Fig. 9, which shows the spatial distribution of ice crystals colored with diameter d_p for different levels of atmospheric turbulence. In the early stages of the vortex regime (until $t = 0.85$ min), the crystals are well-distributed in the primary wake with diameters ranging between 2 and 6 μm . The vortex cores are visible and resemble pictures of vortex tubes (see for example Scorer and Davenport, 1970). Note that regions of low crystal density (i. e. far from the cores) contain larger crystals because, for given ambient supersaturation, the same amount of ambient water vapor has to be shared among less crystals. At the end of the vortex regime ($t = 1.5$ min), the vortex tubes are still visible and the secondary wake has started to form. Crystals remain relatively small in the primary wake while they grow mostly in secondary wake where they are exposed to a supersaturated environment. The presence of atmospheric turbulence folds the structure of the secondary wake and the peripheral regions of the primary wake. At $t = 3$ min, the primary wake is rearranged into a puff as a consequence of the turbulent dissipation that results from the break-up (named induced turbulence hereafter). The figure shows that turbulence increases the mixing of the contrail with ambient air and favors the development of Crow instability. As a consequence, the vertical extension reduces with the turbulence intensity because the vortices tend to destabilize and break up earlier in the case of strong turbulence compared to weak turbulence.

Contrail diffusion is analyzed in Fig. 10 that shows the evolution of the contrail volume per meter of flight V_p normalized by the reference volume $V_{p,0} = 2\pi r_c^2 L_z$. The contrail



LES of contrails in
turbulent atmosphere

J. Picot et al.

Title Page

Abstract

Introduction

Conclusions

References

Tables

Figures

I◀

▶I

◀

▶

Back

Close

Full Screen / Esc

Printer-friendly Version

Interactive Discussion



volume is computed as the sum of elementary volumes containing at least one crystal and defined over a regular mesh with 1 m of resolution. Up to $t = 40$ s, the volume expansion is similar for the three turbulence levels, except for case 6 ($T_0 = 215$ K) where the initial positions of crystals corresponds to a jet regime with a different background temperature. When $T_0 = 218$ K and starting at $t = 40$ s, the volume expands faster with stronger turbulence, as also observed in snapshots of Fig. 9. The figure also reveals the intensity of wake turbulence compared with atmospheric turbulence as the volume expands four times faster in the dissipation regime. It is interesting to note that the expansion rate is the same for all cases at the end of the simulation, even for case 6 ($T_0 = 215$ K). This means that induced turbulence is the major contributor to contrail diffusion in the dissipation regime. Although, atmospheric turbulence is expected to become predominant as wake turbulence dissipates.

Figure 12 shows the evolution of ice mass per meter of flight M_i normalized by the mass of vapor emitted by the engines $M_{v,0} = 15 \text{ g m}^{-1}$. The mass M_i is obtained using Eq. (6)

$$M_i = \frac{1}{L_z} \sum_p n_c m_p = \frac{1}{L_z} \sum_p n_c \frac{\pi}{6} d_p^3 \rho_{ice}. \quad (15)$$

At the beginning of the vortex regime, the emitted water has been completely deposited on crystals, i. e. $M_i = M_{v,0}$. When ambient air is subsaturated (case 5), the ice mass decreases exponentially, consistently with observations of non-persistent contrails. When ambient air is supersaturated (all but case 5), the ice mass reaches a maximum at $t = 25$ s. This maximum indicates that all available vapor (exhaust vapor plus atmospheric vapor trapped in the wake) has been converted into ice so that $s = 100\%$ inside the contrail. As vapor density in the atmosphere scales with s_0 , this maximum is higher when the atmosphere is more supersaturated. In cases 2, 3, 4, and 6, the ice mass decreases from $t = 1$ min to the end of the vortex regime. This decrease indicates the sublimation of crystals, explained by the process of adiabatic compression occurring in the primary wake (Unterstrasser et al., 2008). On the other hand, the mixing of the

LES of contrails in
turbulent atmosphere

J. Picot et al.

Title Page

Abstract

Introduction

Conclusions

References

Tables

Figures

I◀

▶I

◀

▶

Back

Close

Full Screen / Esc

Printer-friendly Version

Interactive Discussion



secondary wake with ambient air (see e. g. Fig. 10) partly compensates sublimation so that the ice mass reduction is less pronounced when increasing the turbulence intensity, and even completely compensates sublimation in case 1. The number of particles surviving the adiabatic compression is an important parameter to consider when evaluating the climate impact of contrails. Figure 11 shows the fraction of surviving crystals, and their values at the end of the simulation are summarized in Table 3 for all considered cases. These data indicate that almost all crystals survive when $s_0 = 1.30$ and 75% survive when $s_0 = 1.10$, which is higher than the results obtained by Unterstrasser and Sölch (2010) and recently by Unterstrasser (2014) and Lewellen et al. (2014). As discussed in Sec. 5, this can be caused by the the different microphysical set-up (cf. inclusion of Kelvin effect) and/or the mixing efficiency predicted by the two models, especially in the peripheral region of the primary wake in Fig. 9. In the dissipation regime, the ice mass grows again as the consequence of induced turbulence. At $t = 4$ min, M_i reaches $2M_{v,0}$ when $s_0 = 110\%$ (case 4), $4.5M_{v,0}$ when $T_0 = 215$ K (case 6), and $8.5M_{v,0}$ when $s_0 = 130\%$, $T_0 = 218$ K and regardless of the turbulence level. The less pronounced increase of ice mass for lower ambient temperature can be understood by observing that ambient saturation is kept constant between cases 2 and 6. Hence, the density of water vapor $\rho_v = s\rho_v^{s,i}(T)$ decreases when decreasing T (since $\rho_v^{s,i}$ is a growing function of temperature). In case 6, the mass of vapor entraining in the contrail and condensing into ice is then reduced compared to case 2 as shown in Fig. 12.

It is interesting to evaluate equilibrium between vapor and ice in the contrail as it can lead to a simpler and less computationally expensive model of microphysics. The equilibrium ice mass M_e represents the mass of ice the contrail would have if all available vapor were deposited onto crystals. It is defined by

$$M_e = M_i + M_{v,a} \quad \text{with} \quad M_{v,a} = \int_{V_p} (\rho_v - \rho_v^{s,i}) dV_p. \quad (16)$$

Figure 13 shows the ratio of deposited mass M_i/M_e . At $t = 25$ s, the ratio is close to one consistently with the equilibrium state suggested earlier in this section. The com-

LES of contrails in turbulent atmosphere

J. Picot et al.

Title Page

Abstract

Introduction

Conclusions

References

Tables

Figures

◀

▶

◀

▶

Back

Close

Full Screen / Esc

Printer-friendly Version

Interactive Discussion



petition between ice sublimation due to the adiabatic compression and ice deposition by mixing of the secondary wake is seen again here at the end of the vortex regime. When turbulence is strong (case 1) deposition is stronger than sublimation as $M_i/M_e \lesssim 1$, whereas when turbulence is weak (case 3) sublimation is stronger than deposition as $M_i/M_e \gtrsim 1$. When supersaturation is reduced to $s_0 = 110\%$ (case 4), sublimation is much stronger than deposition and the equilibrium mass M_e approaches zero (while M_i/M_e diverges). In the dissipation regime, the ratio M_i/M_e reduces due to the mixing produced by the induced turbulence, and reaches a constant value of 0.7 when $s_0 = 130\%$ (regardless turbulence intensity or background temperature) and 0.45 when $s_0 = 110\%$. This result can be explained with an estimation of the rate of change of vapor in the contrail. On one hand, the quantity of vapor is increased by mixing at a rate of $Q_m = s_0 \rho_v^{s,i}(T_0) dV_p/dt$, neglecting temperature variations in the contrail vicinity. On the other hand, the quantity of vapor is decreased by deposition at a rate of $Q_d = n d m_p/dt = C n (s - 1) \rho_v^{s,i}(T_0)$ where C is a constant. The temperature dependence of $G(K n_p) D_{v,p}$ in Eq. (7) can reasonably be neglected in this context. Figure 13 shows that these rates are balanced at the end of the simulation. When T_0 is reduced, both Q_m and Q_d are decreased by the same amount, which does not change the balance (although, the time needed to reach this balance increases). When s_0 is reduced, Q_m is reduced by 15% while Q_d is reduced (through n) by 25%, the balance is then changed towards higher amounts of vapor in the contrail.

The optical thickness of the contrail $\bar{\delta}$ is shown in Fig. 14. It is evaluated by first computing the optical thickness $\delta(S_{xy})$ over each column $S_{xy} = [x, x + \Delta x[\times [y, y + \Delta y[\times L_z$, and averaging δ over the regions where $\delta(S_{xy}) > 0$. Over a column S_{xy} , the optical thickness is computed as follows

$$\delta(S_{xy}) = \frac{1}{\Delta x \Delta y} \sum_{x_p \in S_{xy}} n_c \frac{\pi}{4} d_p^2 Q \left(2\pi(\mu_0 - 1) \frac{d_p}{\lambda_0} \right) \quad (17)$$

where the sunlight is assimilated to a monochromatic wave of wavelength $\lambda_0 = 550\text{ nm}$, the refractive index of water is $\mu_0 = 1.31$, and the extinction coefficient is approximated

by the anomalous diffraction theory (Van De Hulst, 1957)

$$Q(\rho) = 2 - \frac{4}{\rho} \sin \rho + \frac{4}{\rho^2} (1 - \cos \rho). \quad (18)$$

On Fig. 14, when ambient air is not saturated (case 5), $\bar{\delta}$ decreases exponentially and, by 2.5 min, it falls below the threshold $\bar{\delta} < 0.03$ used by Kärcher et al. (1996) as a visibility criterion. Although the visibility of a contrail does depend not only on the optical depth but on many other parameters (angle between observation and sun, contrast against background, aerosols between observer and contrail etc.), the simplistic treatment used here is in line with those employed in previous numerical simulations of contrails (Unterstrasser and Gierens, 2010a; Naiman et al., 2011). When ambient air is supersaturated, $\bar{\delta}$ increases by 25% of the initial value by the time the contrail reaches the equilibrium state. Afterwards, $\bar{\delta}$ decreases by the end of the vortex regime, which is due to the microphysical processes mentioned above combined with the dilution of the contrail that reduces the number density of ice crystals and thus $\bar{\delta}$ in every cases. In case 4 ($s_0 = 110\%$), the more pronounced sublimation results in a stronger reduction of $\bar{\delta}$. In the early stages of the dissipation regime, the mean optical thickness has larger fluctuations due to induced turbulence, as shown in Fig. 9. As the contrail expands and diffuses, these oscillations are damped and the optical thickness attains a value of around 0.06 when $s_0 = 110\%$ (case 4), 0.18 when $T_0 = 215\text{K}$ (case 6), and 0.22 when $s_0 = 130\%$, $T_0 = 218\text{K}$, regardless of the turbulence level. Values of the mean contrail optical thickness of the order of 0.2 to 0.3 were reported by Voigt et al. (2011) and Jeßberger et al. (2013) for the CONCERT campaign and for similar aircraft. Jeßberger et al. (2013) also reported qualitatively similar results with the EULAG-LCM LES model (Sölch and Kärcher, 2010) and the CoCiP model (Schumann, 2012), i. e. $0.05 < \bar{\delta} < 0.1$ in weakly supersaturated atmospheres and $0.1 < \bar{\delta} < 1$ in strongly supersaturated atmospheres. Optical thickness is lower when s_0 or T_0 is reduced as they both reduce density of water in the atmosphere.

Figure 15 compares crystal diameter distributions dn/dd_p with in situ measurements (Schröder et al., 2000). In the simulations, dn/dd_p is computed as

$$\frac{dn}{dd_p}(d; h) = \frac{n_c}{V_p} \text{Part}(d \leq d_p < d + h) \quad (19)$$

where Part (C) is the number of numerical particles satisfying the condition C . Note that dn/dd_p represents an average of the whole contrail whereas measurements are done locally. This may lead to significantly different values where the contrail is highly inhomogeneous such as in the peripheral regions of the contrail with low densities and large crystals. Nevertheless, Fig. 15 shows many common properties between simulations and measurements: the distributions have log-normal shapes which broadens and reduces in density as time advances. When $s_0 = 130\%$ (case 2) the distribution readily shifts towards larger sizes, whereas when $s_0 = 110\%$ (case 4) the distribution do not shifts. Besides a “sublimation tail” appears when $t = 3$ min as a consequence of adiabatic compression. When $s_0 = 95\%$ the sublimation tail appears as soon as $t = 1$ min, the distribution decreases more quickly and shifts towards smaller sizes showing that the contrail sublimates as a whole. Measurements have smaller sizes and larger densities compared to simulations. This difference may be due to the different conditions encountered in the measurements and those used in the present computations, but also from the uncertainty in the number of nucleation sites as the same mass of water has to be shared on a different number of crystals. These data were obtained from different campaigns or independent flight measurements where the ambient conditions and the characteristics of the aircraft generating the contrail could be substantially different from those considered in this study. In more recent campaigns, Jeßberger et al. (2013) carried out time-averaged measurements to reduce effects of contrail heterogeneity and obtained much broader distributions. Compared to the present results, the number of large crystals ($d_p > 2\mu\text{m}$) is equivalent, but they measured an important number of smaller crystals ($d_p < 2\mu\text{m}$) than the present model. This could be due to the limited number of numerical particles and should lead to an underestimation of $\bar{\delta}$.



However, the smaller coefficient $d_p^2 Q (2\pi(\mu_0 - 1) \frac{d_p}{\lambda_0})$ in Eq. (17) reduces this underestimation. Despite these differences, Fig. 15 shows a reasonable agreement in terms of order of magnitude and shape of the crystal diameter distribution.

5 Discussion and conclusions

This study presented the results of three-dimensional large-eddy simulations of contrail evolution in the vortex and dissipation regimes of an aircraft wake immersed in a turbulent atmospheric flow-field. The computational model is based on an Eulerian–Lagrangian two-phase flow formulation where clusters of ice crystals are tracked as they move in the wake. The background turbulence and the initial condition for the contrail at the end of the jet regime were both generated from appropriate simulations. The focus of the study is to evaluate the effects of atmospheric turbulence on the wake dynamics and the contrail properties, and to compare with the effects of ambient humidity and temperature. The results showed a good agreement with numerical and experimental literature work, in terms of descent and lifespan of wake vortices, overall mass of ice produced, and optical depth. Visual patterns of the primary and secondary wakes, Crow instability and the formation of “puffs” also resembled qualitatively those found in observational analysis. The agreement of particle diameter distribution was also acceptable given the large data scatter and uncertainty of both ambient conditions and soot particle emissions in the experimental campaigns compared to those considered in the present study.

The main effect of atmospheric turbulence in the vortex regime is to trigger instabilities in the wake vortices and to accelerate their descent. Stronger turbulence accelerates the onset of the instability, leading to shorter contrail descent and more effective mixing in the interior of the plume. These results are in line with those published in recent wake vortex literature (Holzäpfel et al., 2001; Hennemann and Holzäpfel, 2011; Misaka et al., 2012) and are then a solid basis to investigate their impact on contrail



microphysics. These effects govern the lifetime of the vortices, the vertical extent of the contrail and the number of surviving crystals. Atmospheric turbulence is then an important driver of the contrail evolution in the vortex and dissipation regime, which cannot be captured when the vortex instability is triggered by explicitly forcing one or more modes of the vortex system (Paugam et al., 2010). However, it is found that the self-induced turbulence that is produced in the wake after the vortex break-up dominates over the background turbulence and effectively controls the mixing of the wake with ambient air. As a result, the intensity of the latter has small impact on the microphysical and optical properties on time scales of 4 min after emission. On the other hand, contrail microphysics is strongly influenced by atmospheric temperature and saturation which control the mass of water vapor in contrail surroundings, and the number of surviving crystals. In addition, the mixing induced by the wake turbulence generated during the vortex break-up is able to break the equilibrium between water vapor and ice phases inside the contrail, reducing the mass of ice by more than 30 % compared to model that would enforce equilibrium. Note that, once the wake turbulence has decayed, one can expect that background turbulence would be again the main driver of contrail dynamics in the early diffusion regime. This is the object of current investigation.

The global contrail properties are in line with recent results obtained by numerical simulations that explored a larger set of parameter space (Lewellen et al., 2014; Unterstrasser, 2014). However, for the high supersaturated cases, $s_0 = 1.3$, the present study consistently shows a reduced crystal loss with more than 99% crystals surviving whereas for example Unterstrasser (2014) predicts that 90% crystals survive at $s_0 = 1.4$. As pointed by Lewellen et al. (2014) and confirmed by Unterstrasser (2014), the onset of crystal loss is delayed when the Kelvin effect in the ice growth rate is switched off, which can explain the difference with the present study in which Kelvin effect is not considered. Another factor that can potentially impact the prediction of crystal loss is the treatment of vapor mixing. Indeed, the deposition rate, Eq. (7), depends on the local vapor field which is sensitive to the numerical scheme adopted for scalar advection (Unterstrasser et al., 2014), especially in the zones of high gradients

LES of contrails in turbulent atmosphere

J. Picot et al.

Title Page

Abstract

Introduction

Conclusions

References

Tables

Figures

◀

▶

◀

▶

Back

Close

Full Screen / Esc

Printer-friendly Version

Interactive Discussion



LES of contrails in
turbulent atmosphere

J. Picot et al.

Title Page

Abstract

Introduction

Conclusions

References

Tables

Figures

◀

▶

◀

▶

Back

Close

Full Screen / Esc

Printer-friendly Version

Interactive Discussion



as those occurring in the dissipation regime where the exhausts trapped in the wake is released and mix efficiently with ambient air. Whether it is the microphysical set-up or the order and resolution proprieties of the scalar advection schemes (e.g. high order vs. low order numerical schemes, upwind vs. centered schemes) that is mainly responsible for the difference in the deposition rate and the crystal loss in this phase is a point that deserves further investigation in follow-up studies.

Future work includes a sensitivity analysis of contrail characteristics to the initial number of nucleation sites n . The contrail properties are expected to change throughout its evolution: with increasing n , smaller crystals are expected to be found in the vortex regime as the same mass has to be shared with more crystals, and the contrail is expected to be closer to equilibrium in the dissipation regime as the rate of vapor deposition increases with n in Eq. (4). Finally, the data obtained in this work are being used to reconstruct the initial conditions for the simulations of the diffusion regime and the contrail-to-cirrus transition in an ongoing study. The long term objective is to contribute to the development of subgrid parameterizations for global models that can be used to investigate and evaluate the global radiative effects of contrail cirrus.

Acknowledgements. Financial support from the Direction Général de l'Aviation Civile through the project TC2 (Traînés de Condensation et Climat) is gratefully acknowledged. Computational resources were provided by CINES supercomputing center.

References

- Boivin, M., Simonin, O., and Squires, K. D.: Direct numerical simulation of turbulence modulation by particles in isotropic turbulence, *J. Fluid Mech.*, 375, 235–263, doi:10.1017/S0022112098002821, 1998. 29506, 29507
- Brethouwer, G., Billant, P., Lindborg, E., and Chomaz, J.-M.: Scaling analysis and simulation of strongly stratified turbulent flows, *J. Fluid Mech.*, 585, 343, doi:10.1017/S0022112007006854, 2007. 29504, 29505

LES of contrails in
turbulent atmosphere

J. Picot et al.

Title Page

Abstract

Introduction

Conclusions

References

Tables

Figures

◀

▶

◀

▶

Back

Close

Full Screen / Esc

Printer-friendly Version

Interactive Discussion



Burkhardt, U., Kärcher, B., and Schumann, U.: Global modeling of the contrail and contrail cirrus climate impact, *B. Am. Meteorol. Soc.*, 91, 479–484, doi:10.1175/2009BAMS2656.1, 2010. 29500

Chevalier, H.: Flight Test Studies of the Formation and Dissipation of Trailing Vortices, Tech. Rep. 730295, SAE International, Warrendale, PA, 1973. 29513

Crow, S. C.: Stability theory for a pair of trailing vortices, *AIAA J.*, 8, 2172–2179, doi:10.2514/3.6083, 1970. 29501, 29502, 29512, 29513

Crow, S. C. and Bate, E. R. J.: Lifespan of trailing vortices in a turbulent atmosphere, *J. Aircraft*, 13, 476–482, doi:10.2514/3.44537, 1976. 29511, 29514, 29537

Ducros, F., Comte, P., and Lesieur, M.: Large-eddy simulation of transition to turbulence in a boundary layer developing spatially over a flat plate, *J. Fluid Mech.*, 326, 1–36, doi:10.1017/S0022112096008221, 1996. 29505

Gerz, T. and Ehret, T.: Wingtip vortices and exhaust jets during the jet regime of aircraft wakes, *Aerosp. Sci. Technol.*, 1, 463–474, doi:10.1016/S1270-9638(97)90008-0, 1997. 29501

Gerz, T. and Holzäpfel, F.: Wing-tip vortices, turbulence, and the distribution of emissions, *AIAA J.*, 37, 1270–1276, doi:10.2514/2.595, 1999. 29505

Gerz, T., Dürbeck, T., and Konopka, P.: Transport and effective diffusion of aircraft emissions, *J. Geophys. Res.*, 103, 25905–25913, doi:10.1029/98JD02282, 1998. 29501

Han, J., Lin, Y.-L., Schowalter, D. G., Pal Arya, S., and Proctor, F. H.: Large eddy simulation of aircraft wake vortices within homogeneous turbulence: crow instability, *AIAA J.*, 38, 292–300, doi:10.2514/2.956, 2000. 29513

Hennemann, I. and Holzäpfel, F.: Large-eddy simulations of aircraft wake vortex deformation and topology, *J. Aerospace Eng.*, 25, 1336–1350, 2011. 29513, 29521

Holzäpfel, F.: Probabilistic two-phase wake vortex decay and transport model, *J. Aircraft*, 40, 323–331, 2003. 29514

Holzäpfel, F., Gerz, T., and Baumann, R.: The turbulent decay of trailing vortex pairs in stably stratified environments, *Aerosp. Sci. Technol.*, 5, 95–108, doi:10.1016/S1270-9638(00)01090-7, 2001. 29513, 29521

Huebsch, W. W. and Lewellen, D. C.: Sensitivity studies on contrail evolution, in: 36th AIAA Fluid Dynamics Conference and Exhibit, San Fransisco, California, 5–8 June 2006, doi:10.2514/MFDC06, 2006. 29502

Jeong, J. and Hussain, F.: On the identification of a vortex, *J. Fluid Mech.*, 285, 69–94, doi:10.1017/s0022112095000462, 1995. 29512

LES of contrails in
turbulent atmosphere

J. Picot et al.

Title Page

Abstract

Introduction

Conclusions

References

Tables

Figures

◀

▶

◀

▶

Back

Close

Full Screen / Esc

Printer-friendly Version

Interactive Discussion



- Jeßberger, P., Voigt, C., Schumann, U., Sölch, I., Schlager, H., Kaufmann, S., Petzold, A., Schäuble, D., and Gayet, J.-F.: Aircraft type influence on contrail properties, *Atmos. Chem. Phys.*, 13, 11965–11984, doi:10.5194/acp-13-11965-2013, 2013. 29514, 29519, 29520, 29545
- 5 Kärcher, B., and Yu, F.: Role of aircraft soot emissions in contrail formation, *Geophys. Res. Lett.*, 36, L01804, doi:10.1029/2008GL036649, 2009. 29506, 29507
- Kärcher, B., Peter, T., Biermann, U. M., and Schumann, U.: The initial composition of jet condensation trails, *J. Atmos. Sci.*, 53, 3066–3083, doi:10.1175/1520-0469(1996)053<3066:TICOJC>2.0.CO;2, 1996. 29501, 29508, 29509, 29519, 29545
- 10 Kärcher, B., Busen, R., Petzold, A., Schröder, F. P., Schumann, U., and Jensen, E. J.: Physicochemistry of aircraft-generated liquid aerosols, soot, and ice particles 2. Comparison with observations and sensitivity studies, *J. Geophys. Res.-Atmos.*, 103, 17129–17147, doi:10.1029/98JD01045, 1998. 29507
- Lee, D. S., Fahey, D., Forster, P., Newton, P., Wit, R., Lim, L., Owen, B., and Sausen, R.: Aviation and global climate change in the 21st century, *Atmos. Environ.*, 43, 3520–3537, doi:10.1016/j.atmosenv.2009.04.024, 2009. 29500
- 15 Lele, S. K.: Compact finite difference schemes with spectral-like resolution, *J. Comput. Phys.*, 103, 16–42, doi:10.1016/0021-9991(92)90324-R, 1992. 29506
- Lewellen, D. C. and Lewellen, W. S.: Large-eddy simulations of the vortex-pair breakup in aircraft wakes, *AIAA J.*, 34, 2337–2345, doi:10.2514/3.13399, 1996. 29513
- 20 Lewellen, D. C. and Lewellen, W. S.: The effects of aircraft wake dynamics on contrail development, *J. Atmos. Sci.*, 58, 390–406, doi:10.1175/1520-0469(2001)058<0390:TEOAWD>2.0.CO;2, 2001. 29501, 29502
- Lewellen, D. C., Meza, O., and Huebsch, W. W.: Persistent contrails and contrail cirrus. Part 1: Large-eddy simulations from inception to demise, *J. Atmos. Sci.*, 10.1175/JAS-D-13-0316.1, in review, 2014. 29502, 29503, 29509, 29517, 29522
- 25 Misaka, T., Holzäpfel, F., Hennemann, I., Gerz, T., Manhart, M., and Schwertfirm, F.: Vortex bursting and tracer transport of a counter-rotating vortex pair, *Phys. Fluids*, 24, 025104, doi:10.1063/1.3684990, 2012. 29513, 29521
- 30 Naiman, A. D., Lele, S. K., and Jacobson, M. Z.: Large eddy simulations of contrail development: sensitivity to initial and ambient conditions over first twenty minutes, *J. Geophys. Res.*, 116, D21208, doi:10.1029/2011JD015806, 2011. 29501, 29502, 29503, 29507, 29519

LES of contrails in
turbulent atmosphere

J. Picot et al.

Title Page

Abstract

Introduction

Conclusions

References

Tables

Figures

◀

▶

◀

▶

Back

Close

Full Screen / Esc

Printer-friendly Version

Interactive Discussion



- Paoli, R. and Shariff, K.: Turbulent condensation of droplets: direct simulation and a stochastic model, *J. Atmos. Sci.*, 66, 723–740, doi:10.1175/2008JAS2734.1, 2009. 29503
- Paoli, R., Vancassel, X., Garnier, F., and Mirabel, P.: Large-eddy simulation of a turbulent jet and a vortex sheet interaction: particle formation and evolution in the near field of an aircraft wake, *Meteorol. Z.*, 17, 131–144, doi:10.1127/0941-2948/2008/0278, 2008. 29504
- Paoli, R., Nybelen, L., Picot, J., and Cariolle, D.: Effects of jet/vortex interaction on contrail formation in supersaturated conditions, *Phys. Fluids*, 25, 053305, doi:10.1063/1.4807063, 2013. 29504, 29507, 29510, 29511
- Paoli, R., Thouron, O., Escobar, J., Picot, J., and Cariolle, D.: High-resolution large-eddy simulations of stably stratified flows: application to subkilometer-scale turbulence in the upper troposphere–lower stratosphere, *Atmos. Chem. Phys.*, 14, 5037–5055, doi:10.5194/acp-14-5037-2014, 2014. 29503, 29504, 29511, 29533
- Paugam, R., Paoli, R., and Cariolle, D.: Influence of vortex dynamics and atmospheric turbulence on the early evolution of a contrail, *Atmos. Chem. Phys.*, 10, 3933–3952, doi:10.5194/acp-10-3933-2010, 2010. 29501, 29502, 29503, 29522
- Picot, J., Paoli, R., Thouron, O., and Cariolle, D.: Effects of atmospheric turbulence and humidity on the structure of a contrail in the vortex phase, in: TAC-3 Proceedings, Prien am Chiemsee, 25–28 June 2012, doi:10.2514/MFDC06, 110–113, 2012. 29503
- Pruppacher, H. R. and Klett, J. D.: *Microphysics of Clouds and Precipitation*, vol. 18 of *Atmospheric and Oceanographic Sciences Library*, 2nd edn., Kluwer Academic Publishers, Dordrecht, the Netherlands, 1997. 29508
- Riley, J. J. and Lelong, M.-P.: Fluid motions in the presence of strong stable stratification, *Annu. Rev. Fluid Mech.*, 32, 613–657, doi:10.1146/annurev.fluid.32.1.613, 2000. 29504
- Schröder, F., Kärcher, B., Durour, C., Ström, J., Petzold, A., Gayet, J., Strauss, B., Wendling, P., and Borrmann, S.: On the transition of contrails into cirrus clouds, *J. Atmos. Sci.*, 57, 464–480, doi:10.1175/1520-0469(2000)057<0464:OTTOCI>2.0.CO;2, 2000. 29520, 29546
- Schumann, U.: On conditions for contrail formation from aircraft exhausts, *Meteorol. Z.*, 5, 4–23, 1996. 29501
- Schumann, U.: A contrail cirrus prediction model, *Geosci. Model Dev.*, 5, 543–580, doi:10.5194/gmd-5-543-2012, 2012. 29514, 29519, 29538
- Schumann, U. and Gerz, T.: Turbulent mixing in stably stratified flows, *J. Appl. Meteorol.*, 34, 33–48, 1995. 29505

LES of contrails in
turbulent atmosphere

J. Picot et al.

Title Page

Abstract

Introduction

Conclusions

References

Tables

Figures

◀

▶

◀

▶

Back

Close

Full Screen / Esc

Printer-friendly Version

Interactive Discussion



- Schumann, U., Jeßberger, P., and Voigt, C.: Contrail ice particles in aircraft wakes and their climatic importance, *Geophys. Res. Lett.*, 25, 1336–1350, 2013. 29514
- Scorer, R. S. and Davenport, L. J.: Contrails and aircraft downwash, *J. Fluid Mech.*, 43, 451–464, doi:10.1017/S0022112070002501, 1970. 29515
- 5 Sölch, I., and Kärcher, B.: A large-eddy model for cirrus clouds with explicit aerosol and ice microphysics and Lagrangian ice particle tracking, *Q. J. Roy. Meteor. Soc.*, 136, 2074–2093, doi:10.1002/qj.689, 2010. 29519
- Sonntag, D.: Advancements in the field of hygrometry, *Meteorol. Z.*, 3, 51–66, 1994. 29509
- Spalart, P. R.: On the motion of laminar wing wakes in a stratified fluid, *J. Fluid Mech.*, 327, 139–160, 1996. 29501
- 10 Spalart, P. R. and Wray, A. A.: Initiation of the crow instability by atmospheric turbulence, in: *The Characterisation & Modification of Wakes from Lifting Vehicles in Fluids*, vol. 584, AGARD, Trondheim, 1996. 29514, 29537
- Sussmann, R.: Vertical dispersion of an aircraft wake: aerosol-lidar analysis of en-
trainment and detrainment in the vortex regime, *J. Geophys. Res.*, 104, 2117–2129,
15 doi:10.1029/1998JD200033, 1999. 29501
- Sussmann, R. and Gierens, K. M.: Lidar and numerical studies on the different evolution of vortex pair and secondary wake in young contrails, *J. Geophys. Res.*, 104, 2131–2142, doi:10.1029/1998JD200034, 1999. 29513, 29514
- 20 Tam, C. K. W. and Webb, J. C.: Dispersion-relation-preserving finite difference schemes for computational acoustics, *J. Comput. Phys.*, 107, 262–281, doi:10.1006/jcph.1993.1142, 1993. 29506
- Unterstrasser, S.: Large-eddy simulation study of contrail microphysics and geometry during the vortex phase and consequences on contrail-to-cirrus transition, *J. Geophys. Res.*, 119, 7537–7555, 2014. 29503, 29509, 29517, 29522
- 25 Unterstrasser, S. and Gierens, K.: Numerical simulations of contrail-to-cirrus transition – Part 1: An extensive parametric study, *Atmos. Chem. Phys.*, 10, 2017–2036, doi:10.5194/acp-10-2017-2010, 2010a. 29501, 29502, 29519
- Unterstrasser, S. and Gierens, K.: Numerical simulations of contrail-to-cirrus transition – Part
30 2: Impact of initial ice crystal number, radiation, stratification, secondary nucleation and layer depth, *Atmos. Chem. Phys.*, 10, 2037–2051, doi:10.5194/acp-10-2037-2010, 2010b. 29501

LES of contrails in
turbulent atmosphere

J. Picot et al.

Title Page

Abstract

Introduction

Conclusions

References

Tables

Figures

I◀

▶I

◀

▶

Back

Close

Full Screen / Esc

Printer-friendly Version

Interactive Discussion



Unterstrasser, S. and Sölch, I.: Study of contrail microphysics in the vortex phase with a Lagrangian particle tracking model, *Atmos. Chem. Phys.*, 10, 10003–10015, doi:10.5194/acp-10-10003-2010, 2010. 29502, 29507, 29517

Unterstrasser, S., Gierens, K., and Spichtinger, P.: The evolution of contrail microphysics in the vortex phase, *Meteorol. Z.*, 17, 145–156, doi:10.1127/0941-2948/2008/0273, 2008. 29502, 29516

Unterstrasser, S., Paoli, R., Sölch, I., Kühnlein, C., and Gerz, T.: Dimension of aircraft exhaust plumes at cruise conditions: effect of wake vortices, *Atmos. Chem. Phys.*, 14, 2713–2733, doi:10.5194/acp-14-2713-2014, 2014. 29502, 29522

Van De Hulst, H. C.: *Light Scattering by Small Particles*, Courier Dover Publications, Mineola, NY, 1957. 29519

Voigt, C., Schumann, U., Jeßberger, P., Jurkat, T., Petzold, A., Gayet, J., Krämer, M., Thornberry, T., and Fahey, W.: Extinction and optical depth of contrails, *Geophys. Res. Lett.*, 38, L111806, doi:10.1029/2011GL047189, 2011. 29519, 29545

Widnall, S. E., Bliss, D., and Zalay, A.: Theoretical and experimental study of the stability of a vortex pair, in: *Aircraft Wake Turbulence and Its Detection*, Plenum Press, Seattle, Washington, 305–338, 1970. 29512

Widnall, S. E., Bliss, D. B., and Tsai, C.-Y.: The instability of short waves on a vortex ring, *J. Fluid Mech.*, 66, 35–47, 1974. 29501, 29502

LES of contrails in
turbulent atmosphere

J. Picot et al.

Table 1. Reference values common to all cases. Aircraft data refer to a B747 (4-engines) aircraft. Exhaust jet values are expressed in meter of flight.

Quantity	unit	Value(s)
Computational Domain		
Grid cells		$519 \times 619 \times 100$
Grid spacing $\Delta x \times \Delta y \times \Delta z$	m	$1 \times 1 \times 4$
Domain $L_x \times L_y \times L_z$	m	$1000 \times 1000 \times 400$
Atmosphere		
Brunt–Väisälä frequency N	s^{-1}	0.012
Reference altitude z_0	m	11 000
Reference pressure p_0	Pa	24 286
Wake vortices (B747 data)		
Initial circulation Γ	$\text{m}^2 \text{s}^{-1}$	565
Core radius r_c	m	4
Initial separation b	m	47
Exhaust jets (B747 data)		
Emitted vapor mass $4 \times m_{v,e}$	g m^{-1}	4×3.75
Emitted nucleation sites n_e	m^{-1}	10^{12}

Title Page

Abstract

Introduction

Conclusions

References

Tables

Figures

I◀

▶I

◀

▶

Back

Close

Full Screen / Esc

Printer-friendly Version

Interactive Discussion



LES of contrails in
turbulent atmosphere

J. Picot et al.

Table 2. Table of simulations. The parameter ϵ is the eddy dissipation rate of the background turbulence, η_0 is the relative turbulence intensity, T_0 is the temperature at flight level, and s_0 is the saturation ratio (in the whole domain). Across the following figures, each simulation is represented by a unique symbol or line pattern, which are indicated in this table.

case	ϵ ($\text{m}^2 \text{s}^{-3}$)	η_0	T_0 (K)	s_0	Symbol	& line
1	12.5×10^{-5}	0.095	218	1.30	X	- - - -
2	1.6×10^{-5}	0.048	218	1.30	\diamond	— — —
3	0.57×10^{-5}	0.034	218	1.30	+	— — —
4	1.6×10^{-5}	0.048	218	1.10	Δ	- - - -
5	1.6×10^{-5}	0.048	218	0.95	∇
6	1.6×10^{-5}	0.048	215	1.30	\square	— - -

Title Page

Abstract

Introduction

Conclusions

References

Tables

Figures

I◀

▶I

◀

▶

Back

Close

Full Screen / Esc

Printer-friendly Version

Interactive Discussion



LES of contrails in
turbulent atmosphere

J. Picot et al.

Table 3. Summary of main contrail characteristics: lifespan t_b of wake vortices; fraction of surviving crystals at the end of the vortex regime; and mean optical thickness $\bar{\delta}$ at the end of the vortex regime.

case	Lifespan t_b s	Fraction of surviving crystals at 4 min %	Optical thickness $\bar{\delta}$ at 4 min –
1	95	99.89	0.22
2	132	99.74	0.22
3	111	99.66	0.22
4	132	74.71	0.06
5	132	2.78	< 0.03
6	118	99.71	0.18

Title Page

Abstract

Introduction

Conclusions

References

Tables

Figures

I◀

▶I

◀

▶

Back

Close

Full Screen / Esc

Printer-friendly Version

Interactive Discussion



LES of contrails in
turbulent atmosphere

J. Picot et al.

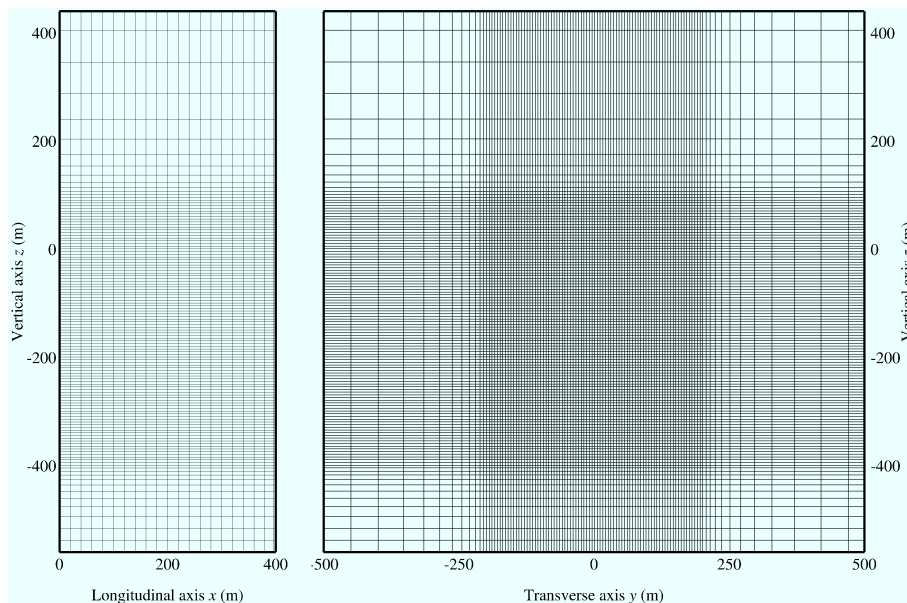


Figure 1. Vertical cross-sections of the computational domain and along the contrail longitudinal axis (left panel) and transverse axis (right panel). The mesh is regular in the subdomain $[0\text{ m}, 400\text{ m}] \times [-200\text{ m}, 200\text{ m}] \times [-350\text{ m}, +100\text{ m}]$. For the sake of clarity 1 out of 5 grid points are shown.

Title Page

Abstract

Introduction

Conclusions

References

Tables

Figures

I◀

▶I

◀

▶

Back

Close

Full Screen / Esc

Printer-friendly Version

Interactive Discussion



LES of contrails in
turbulent atmosphere

J. Picot et al.

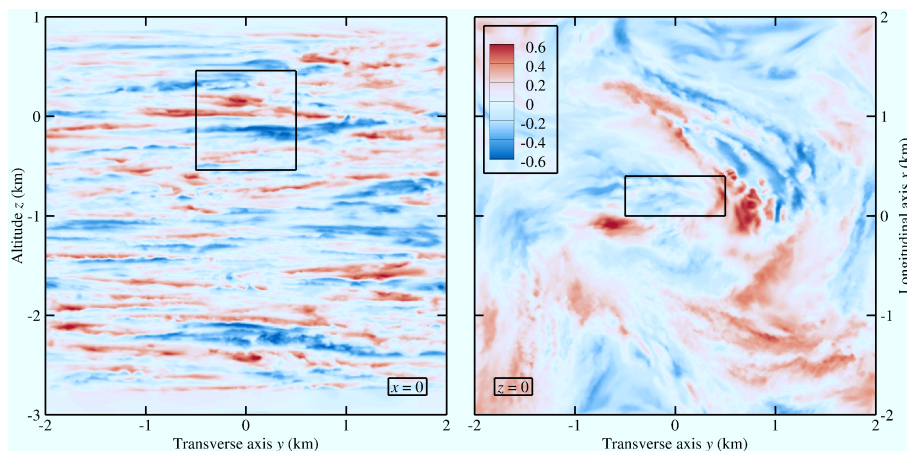


Figure 2. Vertical (left) and horizontal (right) cross-sections of potential temperature difference $\theta - \theta_b$ in K for the atmospheric flow-field used in cases 2 and 4. The data from Paoli et al. (2014) are extracted in the regions delimited by the black boxes and used to initialize the present simulations.

Title Page

Abstract

Introduction

Conclusions

References

Tables

Figures

◀

▶

◀

▶

Back

Close

Full Screen / Esc

Printer-friendly Version

Interactive Discussion



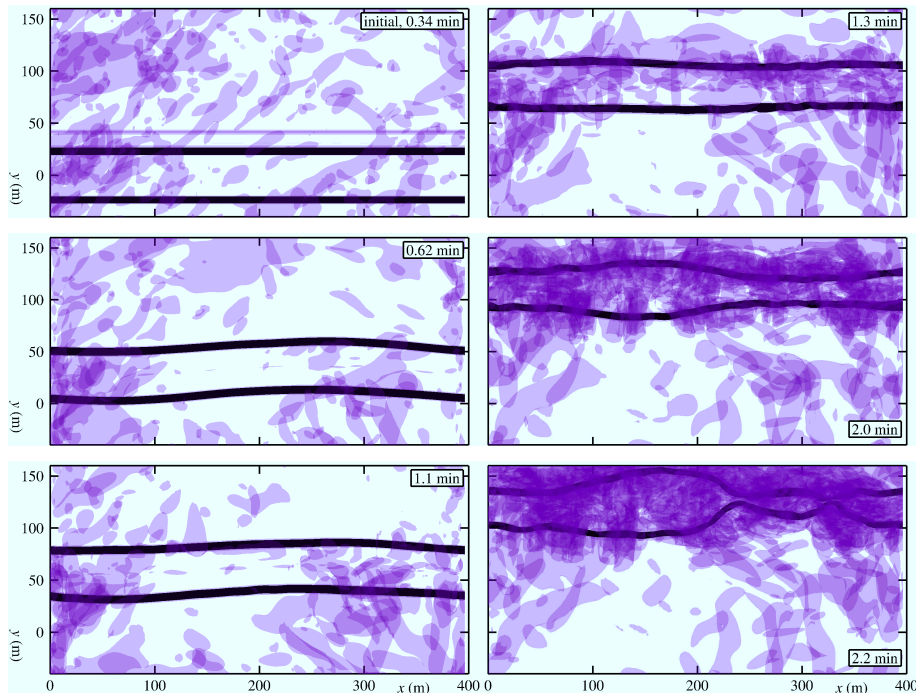


Figure 3. Top views of iso-contours $\lambda_2 = \lambda_{2,0}/10$ (black) and $\lambda_2 = \lambda_{2,0}/400\,000$ (colored) in a horizontal plane xy at different instants for case 2. Black contours show the cores of the trailing vortices whereas the colored contours show the vortical structures of atmospheric turbulence. The development of instabilities is dominated by the long-wave (Crow) instability. The short-wave (elliptical) instability is also visible after $t = 2$ min as well as secondary vorticity structures around each trailing vortex. The displacement of the wake along the y direction is due to the oscillation of a large-scale energetic mode in the background turbulent field.

LES of contrails in
turbulent atmosphere

J. Picot et al.

Title Page

Abstract

Introduction

Conclusions

References

Tables

Figures

I◀

▶I

◀

▶

Back

Close

Full Screen / Esc

Printer-friendly Version

Interactive Discussion

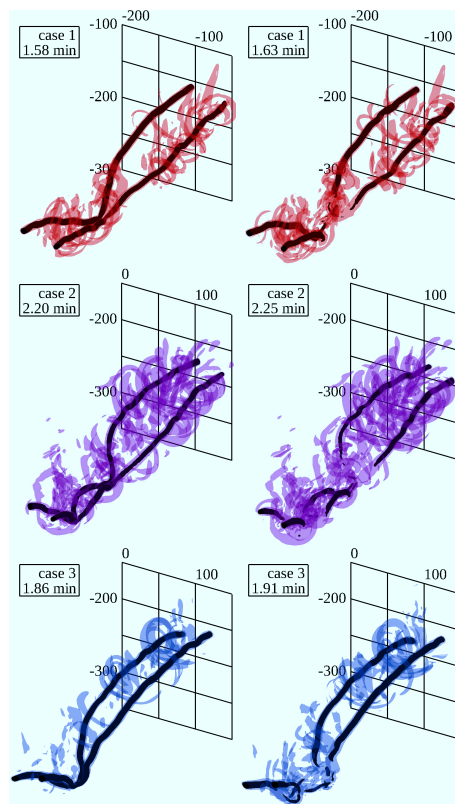


Figure 4. Iso-contours $\lambda_2 = \lambda_{2,0}/10$ (black) and $\lambda_2 = \lambda_{2,0}/1\,000$ (colored) taken immediately before (left panels) and after (right panels) the vortex tubes collide. Black iso-contours represent the wake vortices while colored iso-contours represent the secondary vortices.

LES of contrails in
turbulent atmosphere

J. Picot et al.

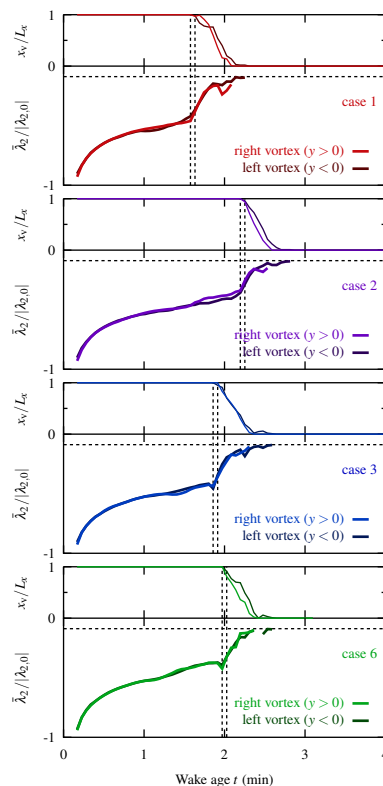


Figure 5. Time histories of vortex length ratios x_v/L_x and $\lambda_2/\lambda_{2,0}$ for cases 1, 2, 3 and 6. The horizontal dashed lines for each case indicate the threshold values $\lambda_2 = \lambda_{2,0}/10$ that is used to discriminate the wake vortex tubes from the background turbulence. The two vertical dashed lines correspond to the times selected in the iso-contours of Fig. 4 (i.e. immediately before and after the vortex break-up) and define the lifespans of the wake vortices.

Title Page

Abstract

Introduction

Conclusions

References

Tables

Figures

◀

▶

◀

▶

Back

Close

Full Screen / Esc

Printer-friendly Version

Interactive Discussion



LES of contrails in
turbulent atmosphere

J. Picot et al.

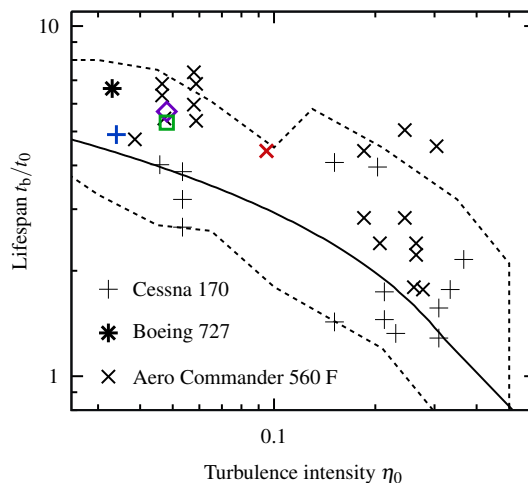


Figure 6. Lifespans of wake vortices as a function of relative turbulence intensity. The solid line is the analytical estimation by Crow and Bate (1976), the dashed line outlines lifespans obtained by numerical simulations of (Spalart and Wray, 1996) and black crosses are in-situ measurements (Crow and Bate, 1976). Simulations: X case 1, \diamond case 2, + case 3, and \square case 6.

Title Page

Abstract

Introduction

Conclusions

References

Tables

Figures

◀

▶

◀

▶

Back

Close

Full Screen / Esc

Printer-friendly Version

Interactive Discussion



LES of contrails in
turbulent atmosphere

J. Picot et al.

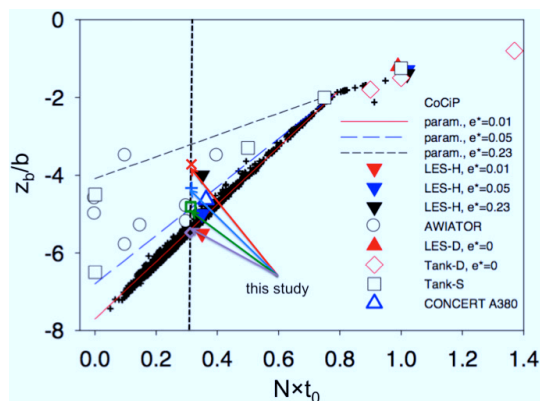


Figure 7. Non-dimensional maximum descent z_b/b of wake vortices as a function of non-dimensional Brunt–Väisälä frequency $N \times t_0$ for the present simulations and a collection of experimental and numerical data (adapted from Schumann, 2012). Simulations: X case 1, \diamond case 2, + case 3, and \square case 6. Note that $z_b/b = w_0 \times t_b/b = t_b/t_0$ with $t_0 = 2\pi b_0^2/\Gamma$. In all cases considered in this study, $t_0 \approx 25$ s and $N \times t_0 \approx 0.3$ (see Table 1).

Title Page

Abstract

Introduction

Conclusions

References

Tables

Figures

◀

▶

◀

▶

Back

Close

Full Screen / Esc

Printer-friendly Version

Interactive Discussion



LES of contrails in
turbulent atmosphere

J. Picot et al.

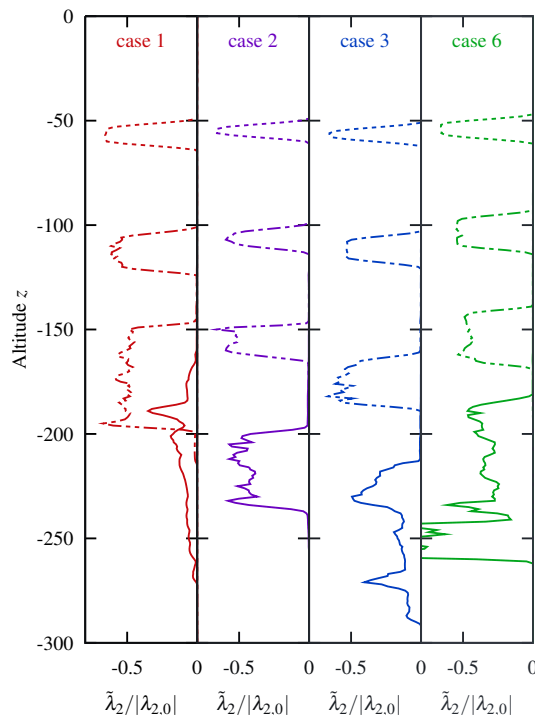


Figure 8. Vertical profiles of $\tilde{\lambda}_2/\lambda_{2,0}$ that is used to track the wake vortices as they move downwards and break up. The four profiles shown for each case correspond to - - - $t = 0.5$ min, - · - $t = 1$ min, - - - $t = 1.5$ min, — $t = 2$ min.

Title Page

Abstract

Introduction

Conclusions

References

Tables

Figures

◀

▶

◀

▶

Back

Close

Full Screen / Esc

Printer-friendly Version

Interactive Discussion



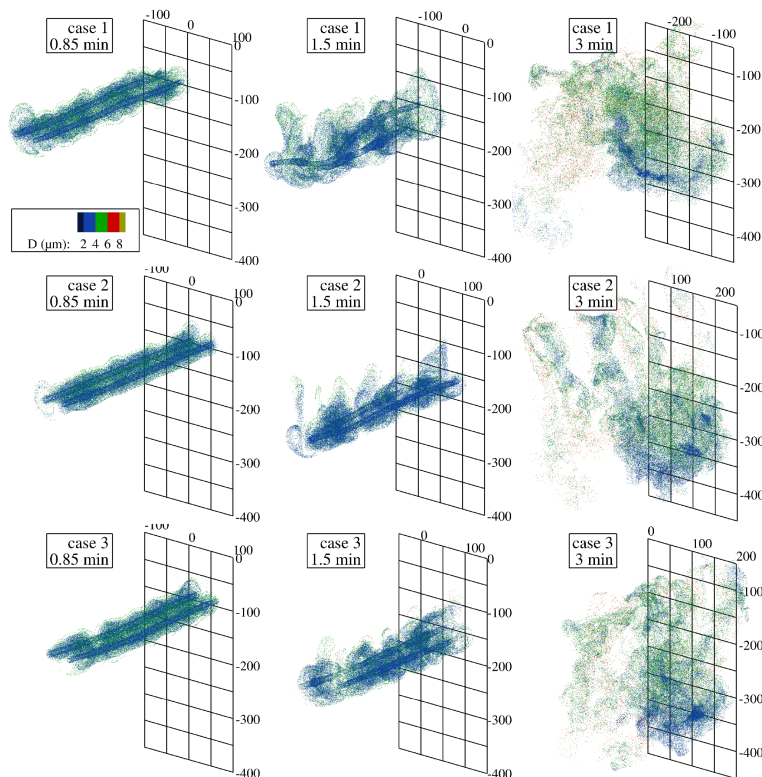


Figure 9. Snapshots of ice crystals spatial distribution for cases 1, 2, and 3. Crystals are colored with diameters. The figure shows the development of the secondary wake at $t = 1.5$ and 3 min (center and right panels) and the formation of puffs at $t = 3$ min (right panels). It can be observed that the size of crystals slightly increases during the instability process of the vortex regime ($t \leq 1.5$ min) whereas it increases considerably in the dissipation regime ($t = 3$ min) with larger crystals found in the secondary wake. Crystals appear more mixed in the strong atmospheric turbulence case (top panels).

LES of contrails in
turbulent atmosphere

J. Picot et al.

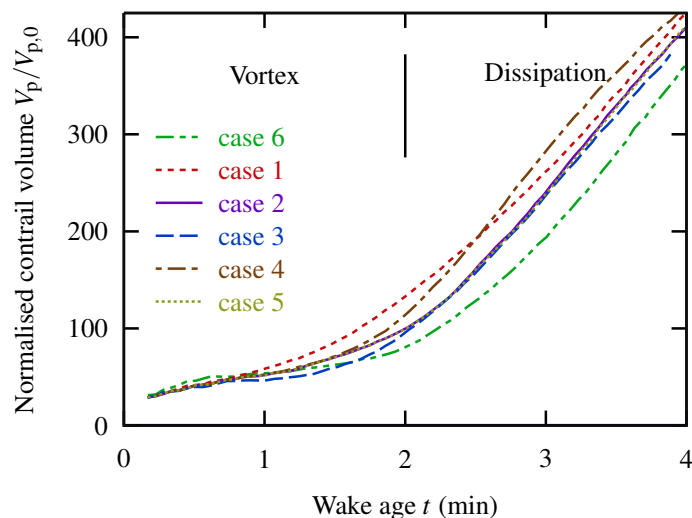


Figure 10. Normalized contrail volume per meter of flight. Note the increased mixing following the vortex the break-up where the exhaust material is released into the atmosphere and the expansion rate of the contrail volume increases by a factor of 4.

Title Page

Abstract

Introduction

Conclusions

References

Tables

Figures

◀

▶

◀

▶

Back

Close

Full Screen / Esc

Printer-friendly Version

Interactive Discussion



LES of contrails in
turbulent atmosphere

J. Picot et al.

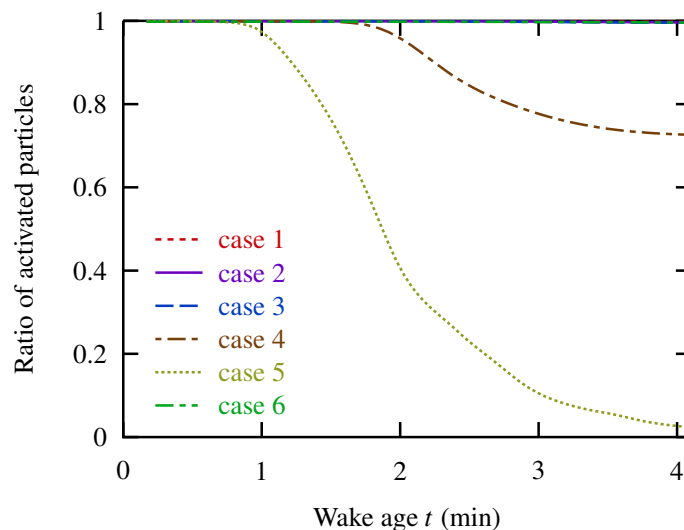


Figure 11. Normalized number of activated particles (fraction of surviving crystals). Adiabatic compression is strong enough in weakly supersaturated atmosphere (case 4) to completely sublime 30 % of crystals, but it is not able to evaporate any crystals in strongly supersaturated atmosphere.

Title Page

Abstract

Introduction

Conclusions

References

Tables

Figures

◀

▶

◀

▶

Back

Close

Full Screen / Esc

Printer-friendly Version

Interactive Discussion



LES of contrails in
turbulent atmosphere

J. Picot et al.

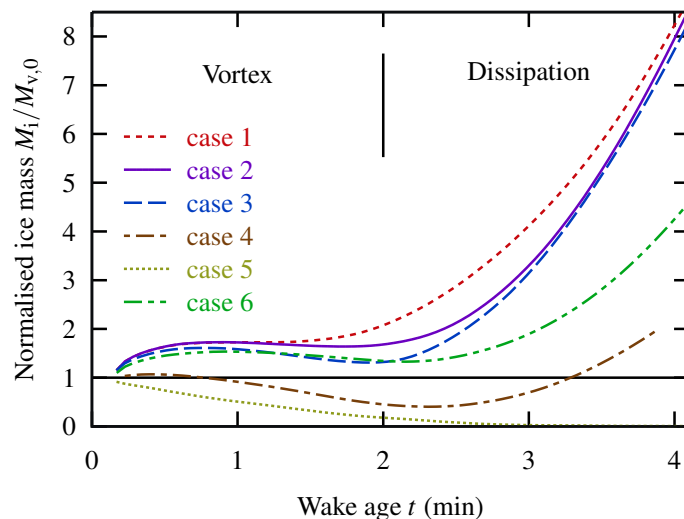


Figure 12. Ice mass per meter of flight normalized by the mass of emitted water vapor. Adiabatic compression reduces M_i at the end of the vortex regime, and this is particularly effective when the atmosphere is weakly supersaturated (case 4). The break-up of the vortices causes M_i to increase at a rate that depends on atmospheric temperature, saturation, and, to a much lesser extent, on the atmospheric turbulence.

Title Page

Abstract

Introduction

Conclusions

References

Tables

Figures

◀

▶

◀

▶

Back

Close

Full Screen / Esc

Printer-friendly Version

Interactive Discussion



LES of contrails in turbulent atmosphere

J. Picot et al.

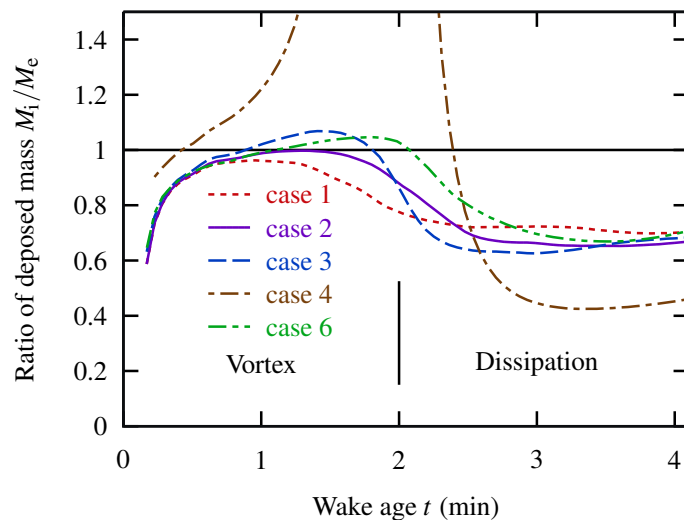


Figure 13. Ratio of deposited mass. In the vortex regime, the contrail is close to equilibrium ($M_i \approx M_e$) only when the atmosphere is strongly supersaturated. In the dissipation regime, the strong mixing between the contrail and ambient air causes a depart from the equilibrium state ($M_i < M_e$).

Title Page

Abstract

Introduction

Conclusions

References

Tables

Figures

◀

▶

◀

▶

Back

Close

Full Screen / Esc

Printer-friendly Version

Interactive Discussion



LES of contrails in turbulent atmosphere

J. Picot et al.

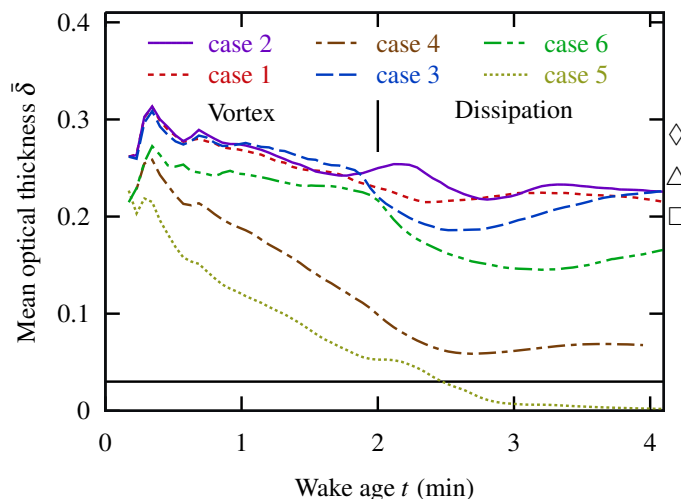


Figure 14. Mean optical thickness. The horizontal black line represent the visibility criterion $\bar{\delta} > 0.03$ (Kärcher et al., 1996). The mean optical thickness decreases during the vortex regime and stabilizes during the dissipation regime. Its evolution depends mainly on atmospheric temperature and saturation and, to a lesser extent, on atmospheric turbulence. The symbols on the right of the figure shows the values of the optical thickness for different aircraft and atmospheric situations measured in the CONCERT campaign (Voigt et al., 2011) as reported by Jeßberger et al. (2013).

Title Page

Abstract

Introduction

Conclusions

References

Tables

Figures

◀

▶

◀

▶

Back

Close

Full Screen / Esc

Printer-friendly Version

Interactive Discussion



LES of contrails in
turbulent atmosphere

J. Picot et al.

Title Page

Abstract

Introduction

Conclusions

References

Tables

Figures

◀

▶

◀

▶

Back

Close

Full Screen / Esc

Printer-friendly Version

Interactive Discussion

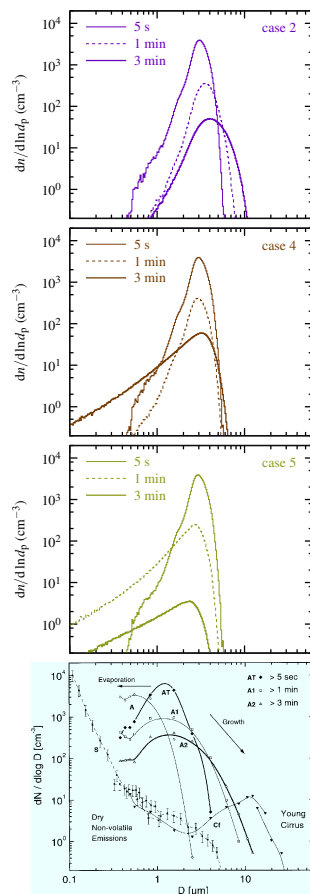


Figure 15. Crystal diameter distributions at 5 s, 1 min, 3 min for the three levels of saturation and measurements from (Schröder et al., 2000) (bottom).